Measurement of neutron total cross sections up to 560 MeV

W. P. Abfalterer,[1] F. B. Bateman,[1] F. S. Dietrich,[2] R. W. Finlay,[3] R. C. Haight,[1] and G. L. Morgan[1]

[1]*Los Alamos National Laboratory, Los Alamos, New Mexico 87545*
[2]*Lawrence Livermore National Laboratory, Livermore, California 94551*
[3]*Ohio University, Athens, Ohio 45701*

We have completed a new set of total cross section measurements of 31 elements and isotopes spanning the periodic table from $A=1$ to 238. We employed the same technique as in Finley *et al.* [Phys. Rev. C **47**, 237 (1993)] with refinements intended to allow measurements on separated isotopes and improved systematic error control. The goal of the new measurement was 1% statistical accuracy in 1% energy bins with systematic errors less than 1%. This was achieved for all but the thinnest samples. Stringent checks of systematic errors in this measurement resulted in a reassignment of systematic uncertainties to the neutron total cross sections reported in Finley *et al.* Microscopic optical model calculations were carried out to interpret the results of the experiment. Two specific types of optical models were employed. The Jeukenne-Lejeune-Mahaux model was used in the range of 5–160 MeV, and a model based on the empirical effective interaction of Kelly was used from 135 to 650 MeV. These models are shown to be useful for predicting both neutron total cross sections and proton reaction cross sections. They are particularly important for light nuclei, for which standard global phenomenological parametrizations of the optical potential are insufficiently accurate.

I. INTRODUCTION

The neutron total cross section is a basic quantity describing the interactions of neutrons with nuclei. If there is any interaction at all, including elastic and all nonelastic interactions, then it is reflected in the total cross section. Yet the database of total cross sections has significant uncertainties and, in regions, significant gaps. Therefore we undertook this extensive program to measure these cross sections.

These measurements were supported by the Accelerator Production of Tritium (APT) project as part of a program to improve the physics in the modeling code (MCNPX) used in the design of the APT target and other parts of the facility. The new data, along with those of Ref. [1], are being used in the development of a global optical potential from 20 to 2000 MeV, testing microscopic folding optical models, and in the development of a simple parametrization of the total cross sections based on Ramsauer-Glauber models [2–4]. The goal of the new measurements was 1% statistical accuracy in 1% energy bins with systematic errors less than 1%. This was achieved for all but the smallest samples, for which the statistical and systematic uncertainties were as large as 3.7% in 1% energy bins as in the case of ^{13}C.

The neutron total cross sections of the 31 materials listed below were measured at the Los Alamos WNR spallation source. We employed the same techniques as in Ref. [1], with refinements intended to allow measurements on separated isotopes and other materials only available in small quantities.

Samples were the APT spallation target material W; medium-mass structural materials Ti, V, Cr, Mn, Fe, Co, and Ni; the actinides Th and depleted U; materials for global optical model development, F, Mg, P, S, K, Y, Mo, In, Au, Hg, and natural Pb; light nuclei Li, B, and C; and separated isotopes of light nuclei ^{6}Li, ^{7}Li, ^{10}B, ^{11}B, and ^{13}C. We are in the process of finalizing results for the medium- and

heavy-mass separated isotopes ^{54,56}Fe (from ^{54,56}Fe$_2$O$_3$) and ^{182,184,186}W, ^{183}W (from ^{183}WO$_3$), and these will be presented in a later paper. The results for the hydrogen isotopes H (from C$_8$H$_{18}$ and CH$_2$), D (from D$_2$O), and the total cross section difference deuterium-hydrogen (D-H) have been presented in Ref. [5], together with Faddeev calculations of the D total cross section. In this paper we describe the techniques and systematic errors that apply to the entire set of measurements.

Total neutron cross sections are determined by measuring the transmitted neutron beam through a known amount of sample material and comparing this with the transmitted beam without sample. If N_o is the number of counts without a sample and N_i is the number of counts with a sample interposed between neutron source and detector, then the transmission is given by

$$T = \frac{N_i}{N_o} = e^{-nl\sigma_T}, \tag{1.1}$$

where n denotes the number of atoms per unit volume and l the sample length. The total neutron cross section σ_T can then be determined as

$$\sigma_T = -\frac{1}{nl}\ln\frac{R_i - B_i}{R_o - B_o}. \tag{1.2}$$

R_i and R_o denote the sample-in and sample-out counts in a given time bin per beam monitor count, respectively, and B_i, B_o the background counts per beam monitor count.

Therefore, for a successful total neutron cross section measurement the following ingredients are needed: an accurate measurement of the areal density (nl), knowledge of the background rates, and an accurate normalization of sample-in and sample-out fluences. Thus we required a well-defined experimental geometry, well-characterized samples,
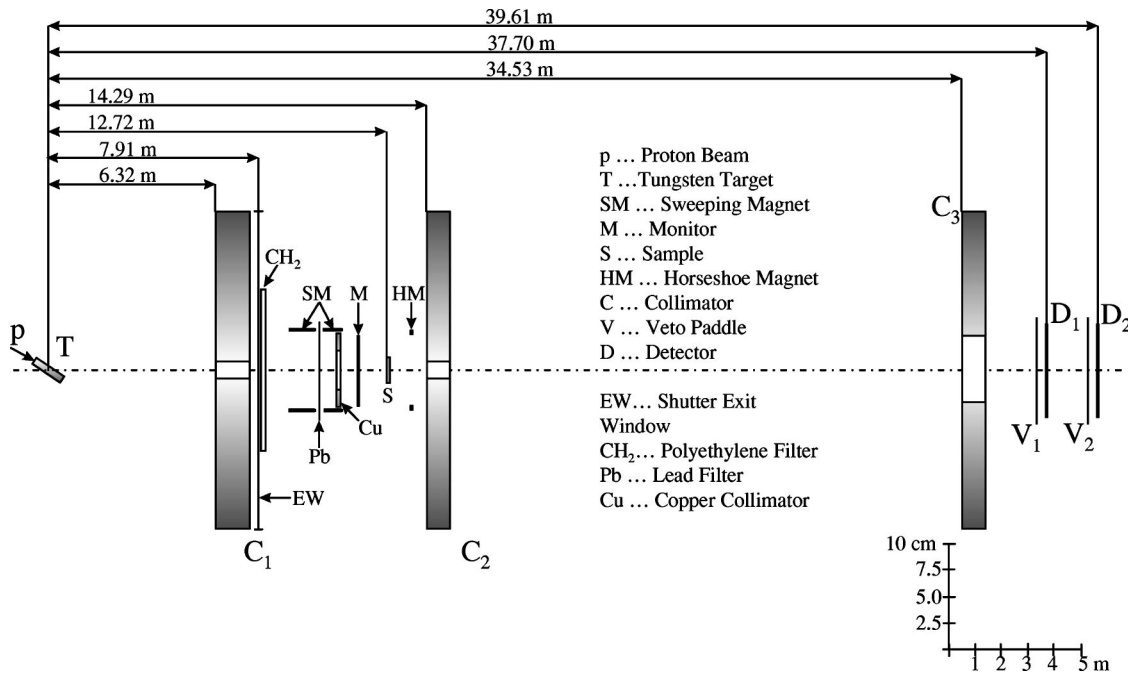
FIG. 1. Experimental geometry (plan view). Elevation view is the same except for the orientation of the tungsten target which is directed slightly upwards at an 8° angle with respect to the horizontal.

a method to determine neutron energies, stable detectors and electronics, and a solid understanding of systematic effects such as electronic dead time.

II. TECHNIQUE

Total cross sections were measured in a good-geometry (i.e., a tightly collimated geometry that minimizes in-scattering) transmission experiment with neutrons up to approximately 600 MeV emanating at 30° from the LANSCE WNR target 4 white (i.e., continuous energy) neutron source [6]. The white neutron source was realized by bombarding a water-cooled tungsten target with 800 MeV protons.

The proton beam time structure was as follows: Protons were bunched to less than 1 ns bunches separated by 1.8 μs, commonly referred to as micropulse spacing. Micropulses were delivered for a period of 625 μs (referred to as the beam gate length), at a 100-Hz repetition rate (referred to as the macropulse rate). Average current to the target was 2 μA. The neutron energy was determined by standard time-of-flight techniques. For further details on the time-of-flight technique see [1,7].

This experiment is distinguished from that in Ref. [1] in a number of ways. Instead of one detector, two detectors were employed with different thicknesses in order to increase the count rate at the high end of the neutron spectrum and also to have a check on systematic errors. Our count rate was further increased by a factor of 2.5 because of an increased macro-pulse repetition rate (100 Hz instead of 40 Hz).

The experimental geometry is shown in Fig. 1. For a more detailed description of the technique used see [7]. Neutrons traveled from the tungsten production target through vacuum to the shutter exit window and then through air for the remainder of the flight path.

A 10.16-cm-thick piece of polyethylene (CH_2) placed in front of the shutter exit window was used to harden the beam for all but the hydrogen and deuterium cross section measurements. This greatly reduced the overall count rate in the detectors but had little effect on the rates above 100 MeV where high statistical accuracy is the most difficult to achieve. A 1.27-cm-thick piece of lead was used to attenuate the gamma burst. Two sets of sweeping magnets removed charged particles upstream of the sample. A horseshoe magnet swept charged particles out of the flight path immediately after the sample. The sample currently in the counting position on the 63.5-cm-diam, eight-position sample wheel was situated in such a way as to completely shadow the detectors. Sample diameters were typically 2.54 cm, but spanned a range from 2.117 to 3.810 cm.

Data were taken in 25 sets referred to as ''wheels''; these were distinguished by the samples mounted on the rotating sample changer. In order to assess the stability of the monitor we checked on a run-by-run basis the ratio of sample-out detector to monitor and discarded data taken during the infrequent erratic beam conditions. The overall stability of the monitor was found to be excellent; more details are shown in [7].

To quantify the background and in-scattering effects, the transmission through a 122-cm-long, 2.86-cm-diam oil hard-ened tool steel shadow bar for detectors 1 and 2 was compared with the dead-time-corrected and normalized open beam (sample-out) spectrum (see Fig. 2). The open-beam and shadow bar spectra were normalized to the same number of monitor counts. The size of the peak at channel number ≈ 5200 is consistent with the transmission calculated through the shadow bar. This result shows that backgrounds are small.
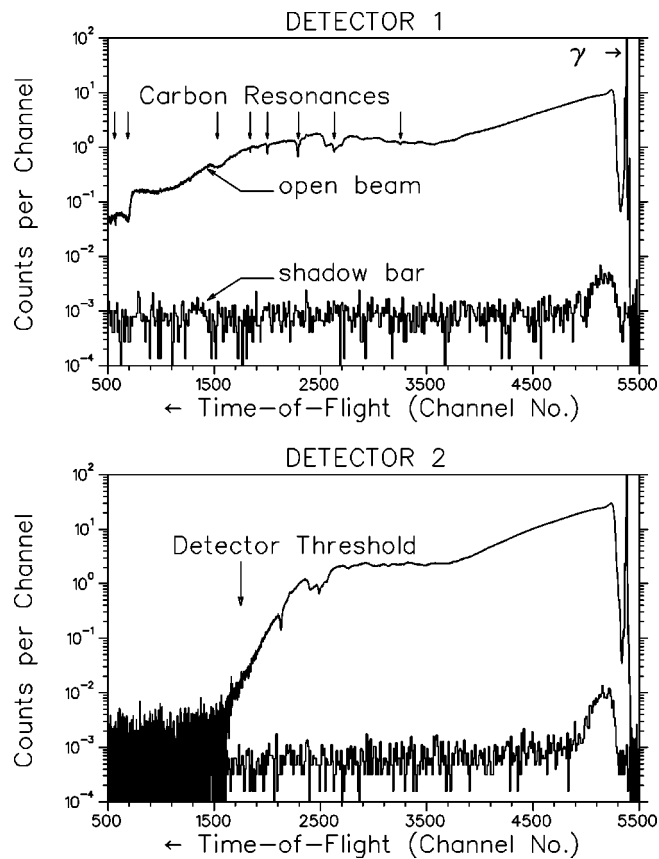
FIG. 2. Open beam (i.e., sample-out) and shadow bar time-of-flight spectra after dead-time corrections for detectors 1 and 2. These show, from right to left, the gamma flash, the fast neutron spectrum modified at the lower energies by transmission resonances in carbon (CH_2 filter), the detector threshold, and the time-independent background. Because of the threshold settings, the last two quantities are visible for detector 2 only. The open-beam and shadow bar spectra were normalized to the same number of monitor counts. The shadow bar time-of-flight spectra are shown averaged in ten-channel bins.

A clear understanding of the systematic uncertainties involved is very important for measuring the neutron total cross sections of very thin samples. For this reason we used two independent detector systems. The detectors were distinguished by different thicknesses, bias settings, different types of discriminators, and considerably different count rates for a given sample.

Detector 1 was a 8.9×8.9 cm, 1.27-cm-thick slab of BC404. Detector 1 was located at 37.70±0.01 m from the neutron source as determined by the time difference of the gamma peak and carbon resonances with known energies. Detector 2 was of the same construction, the thickness of the scintillator being 5.08 cm instead. Detector 2 was located at 39.61±0.02 m. The bias on detectors 1 and 2 was set with a constant fraction and leading edge discriminator, respectively.

Veto counters just in front of the neutron detectors were used to reject charged particles produced by neutron reactions on air in the flight path or other materials upstream of each detector. These counters were 0.16- and 0.64-cm-thick
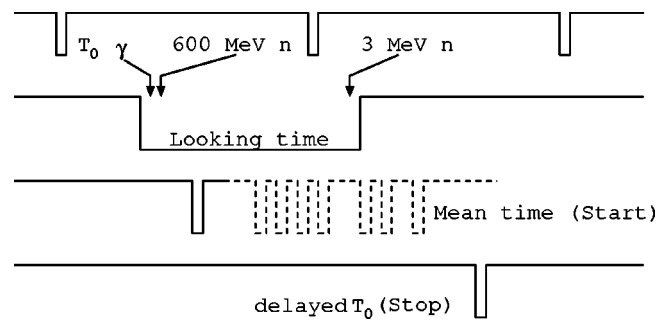

FIG. 3. Simplified timeline showing the logic T_0's associated with the proton beam bursts that arrive at evenly spaced 1.8-μs time intervals, defining a time frame 1.4 and 1.6 μs long (Looking time) for detector 1 and detector 2, respectively. Starts associated with valid neutron or gamma events arrive at a time determined by the mean time of pulses from the two phototubes viewing each detector. For each time frame, a delayed copy of the T_0 defining it was used as a stop signal on the TDC clocks.

plastic scintillator paddles, for detectors 1 and 2, respectively. The monitor counter consisted of a circular plastic scintillator, 5.08 cm diameter and 0.159 cm thick.

Good agreement (better than 1% in the calculated cross sections) between results from detectors 1 and 2 gave confidence in the approach. The overall performance of the two detectors was investigated by varying the thickness of a particular type of sample. Finally, as a check on the long-term stability of the system several samples were remeasured as far apart as half a year, and again excellent agreement was obtained.

III. ELECTRONICS AND DATA ACQUISITION

We describe here the essential principles of the electronics. Figure 3 shows a simplified time line. Logic pulses (referred to as T_0) associated with the proton beam burst arrived at evenly spaced 1.8 μs time intervals. These were used to define a time frame 1.4 and 1.6 μs long for detector 1 and detector 2, respectively. For each time frame, a delayed copy of the T_0 defining it was used as a stop signal on the time-to-digital converter (TDC) clocks. We checked for a busy condition at the beginning of a time frame. If the system was not busy, then it was free to start the clock with a neutron event. This arrangement allowed a clean separation of dead time corrections: (i) ''analytic'' dead time—a neutron event within a frame prevents subsequent events *within that frame* from being analyzed—and (ii) a correction $T_0/T_{0\,live}$ for busy frames.

The complete electronics setup is discussed in [7]. High and low thresholds on neutron energy for detector 1 were set to give useful data above 2.7 and 8 MeV, respectively. The detector 2 threshold was set to yield useful data above E_n = 10 MeV. No high bias was set for detector 2. The data corresponding to the high bias for detector 1 were used only for systematic error checks; cross section results were found to be in excellent agreement with those from detector 2. In the final data analysis, detector 1 was used above a neutron energy where the statistical uncertainty was better than 1%,

TABLE I. Sample characteristics. Densities are known to better than 0.5% for all samples other than ^{10}B (0.8%), ^{11}B (1.6%), ^{13}C (3.7%), and Mn (1.1%).

Sample name	Mass (g)	Length (cm)	Diameter (cm)	Density (g/cm)^3	Mol. weight (g/mol)	1/nl (b/mol [a])	Abund. (%)
^{6}LiH	61.73	18.43	2.484	0.691	6.0594	0.938	^{6}Li: 95.58
							^{7}Li: 4.42
LiF	83.70	19.99	2.258	1.046	25.939	2.061	
^{7}LiH	72.96	18.42	2.540	0.785	6.9950	0.930	^{6}Li: 2.21
							^{7}Li: 97.9
^{10}B	72.37	4.820	3.760	1.344	10.013	2.551	^{10}B: 94.95
							^{11}B: 5.05
B	85.97	20.00	2.258	1.073	10.811	0.836	
^{11}B	32.02	1.999	3.810	1.446	11.010	6.509	^{10}B: 2.85
							^{11}B: 97.15
C	17.80	2.005	2.550	1.744	12.011	5.723	
C	41.50	4.535	2.550	1.799	12.011	2.445	
C	65.33	7.211	2.548	1.782	12.011	1.552	
C	79.50	9.012	2.542	1.746	12.011	1.273	
^{13}C	40.96	3.244	3.500	1.239	13.003	5.072	^{13}C: 98.0
CF$_2$	170.67	15.11	2.540	2.229	50.008	2.466	
CF$_2$	171.69	15.14	2.540	2.238	50.008	2.450	
Mg	88.26	10.06	2.537	1.736	24.305	2.307	
S	86.13	20.00	2.255	1.078	32.070	2.470	
P	90.50	20.00	2.251	1.137	30.974	2.262	
KF	122.57	20.00	2.258	1.530	58.097	3.152	
CaF$_2$ [b]	326.61	20.35	2.543	3.161	78.075	2.016	
Ti	268.86	10.29	2.720	4.506	47.880	1.715	
V	308.76	10.02	2.540	6.100	50.942	1.384	
Cr	167.05	10.00	2.258	4.172	51.996	2.070	
Mn	316.08	19.84	2.253	3.840	54.938	1.151	
Fe	182.30	4.590	2.539	7.843	55.847	2.576	
Ni	457.80	10.03	2.560	8.909	58.690	1.091	
Co	162.88	3.625	2.548	8.812	58.933	3.064	
Y	228.49	10.03	2.542	4.498	88.906	3.274	
Mo	429.80	10.16	2.300	10.22	95.940	1.534	
In	375.52	10.38	2.513	7.287	114.82	2.520	
W	996.90	10.23	2.540	19.19	183.85	1.555	
Au	972.80	10.10	2.525	19.26	196.97	1.681	
Hg	786.75	10.16	2.690	13.63	200.59	2.406	
Pb	572.90	10.22	2.510	11.34	207.20	2.969	
Th	580.37	10.00	2.520	11.66	232.04	3.311	
^{238}U	826.30	10.02	2.520	18.96	238.05	2.080	

[a]Denotes barns per atom or molecule depending on the sample.

[b]This sample was measured in [1]; the neutron total cross section of natural Ca was extracted using the fluorine cross section from this measurement.

typically 3–6 MeV ($\approx$6 MeV in the case of the H samples) depending on the sample. Detector 2 was used above 10 MeV.

Rapid sample cycling was employed to minimize the effects of drifts in the beam spatial and energy profiles. A timing circuit enabled the data acquisition for a 20-s period, after which the wheel on which the samples were mounted was rotated and another sample (or open beam position) investigated.

IV. SAMPLE CHARACTERISTICS

We dealt with several categories of samples: metallic samples, encapsulated natural powder samples, encapsulated isotopic powders, encapsulated isotopic solids, encapsulated liquids, pressed powders, solid hydrogen and fluorine compounds, and sintered samples. All samples were cylindrical. A detailed description of the sample characteristics is presented in [7]. Tables I, II, and III summarize the characteristics of the samples reported in this paper.

TABLE II. Liquid hydrogen and fluorine compounds. A temperature monitoring system was set up during the liquid carbon compound and water runs. The density variation with temperature was taken into account in the cross section determination. The two octane samples listed are the same sample, but as a check on our method for taking into account temperature variations, two sets of data were taken for this sample with different average temperatures. Air bubbles allowed for expansion of the liquids. We assumed the length of the aluminum cylinders containing the sample liquids remained constant independent of temperature. The thermal expansion coefficient of aluminum is 22.5×10^{-6} cm/cm/°C, which resulted in a $\Delta l/l$ for our temperature range covered (typically 10 °C) of 0.02%, and was therefore neglected.

Sample name	Mass (g)	Length (cm)	Diameter (cm)	$\bar{T}$ (°F)	Density (g/cm^3)	Mol. weight (g/mol)	$1/nl$ (b/mol)
C_8H_{18}	343.75	62.04	3.205	61	0.705	114.23	4.334
C_8H_{18}	343.75	62.04	3.205	53	0.709	114.23	4.311
H_2O	395.57	49.69	3.205	52	0.999	18.015	0.6024
D_2O	438.22	49.65	3.205	52	1.106	20.028	0.6059
C_8F_{18}	207.88	14.99	3.200	51	1.775	438.05	27.34

Uncertainties in the areal density of the samples are in several instances the main contributing factor to the systematic uncertainty in the determination of the final total neutron cross sections. Areal density was therefore determined in as many as three ways: by physical measurements of mass and dimensions, by a bulk density measurement by water immersion coupled with a length measurement, and by gamma-ray attenuation.

In addition, a chemical analysis was performed on the liquid samples C_8H_{18} and C_8F_{18}. These analyses showed a negligible level of impurities of other hydrocarbons or fluorocarbons.

V. DATA ANALYSIS

Raw spectra were first processed by applying the socalled analytic dead-time correction. This correction arises from the fact that low-energy neutrons have a smaller probability of being counted than high-energy neutrons because the first-arriving TDC start pulse within a given time frame blocks the system from processing later events within that time frame. Reference [8] gives a detailed description of this effect and the necessary corrections for it.

The remaining dead time of the TDC system is taken care of by scaling the total number of logic T_0's, the number of T_0's while the system was alive (called $T_{0\,live}$), and the number of times a conversion in progress was aborted by a veto-counter event (denoted v). The correction was accomplished by multiplying the analytic-dead-time-corrected data by the factor $T_0/(T_{0\,live}-v)$.

Using charged-particle veto counters results in systematic changes in cross sections that are typically in the 0.5% range compared to data without veto counters. However, it is necessary to correct for accidental coincidences between the veto and main detectors in order to avoid a count-ratedependent systematic error. This was done in all cases where this effect is important.

The time-independent background was then subtracted from the corrected spectra and time of flight converted to energy. For the time-to-energy transformation well-known carbon resonances were used to determine the flight path for detector 1 and detector 2 (see [7]).

Finally, spectra were normalized to the monitor counts, and the total neutron cross section was calculated with all statistical uncertainties properly propagated. The cross section data were prepared in both a channel-by-channel representation and also in 1%-wide energy bins.

VI. SUMMARY OF SYSTEMATIC EFFECTS

A. Beam effects

Throughout the experiment we monitored the neutron time-of-flight spectrum for micropulse contamination, which manifests itself in the form of side lobes on either side of the main gamma peak separated by 5 ns. Whenever the integrated area of the two side peaks approached 1% of the main peak, we demanded a beam tuning adjustment. Typically we were able to keep this contamination to about 0.6%. If the proton bunching were misadjusted and allowed a small continuous stream of protons (''dark current'') across a time frame in addition to the main pulse, then it would be impossible to assign neutron energies because of a lack of precise timing information. This would not be a problem if this trickle were constant in time because then it would just show

TABLE III. Solid hydrogen compounds.

Sample name	Mass (g)	Length (cm)	Diameter (cm)	Density (g/cm^3)	Mol. weight (g/mol)	$1/nl$ (b/mol)
CH_2-50 cm	371.63	50.00	3.185	0.936	14.027	0.499
CH_2-A	185.48	24.96	3.185	0.936	14.027	1.001

up in the neutron time-of-flight spectrum as a constant background, which is easily dealt with. A distortion of the time-of-flight spectrum would be the consequence if the dark current were not constant in time, introducing a time-dependent background, and thereby leading to erroneous total neutron cross sections. A third type of beam contamination, also referred to as ''dark current,'' has a period of 60 ns and is caused by a mistuning of the buncher. Very occasionally this contamination was observed, but this was at a very low level. Again, when this was observed, the operators were asked to retune the buncher. In our final cross section data there are no observable features corresponding to such 60-ns artifacts. As noted earlier, we checked the background as seen by the detectors by inserting a shadow bar into the flight path (see Fig. 2), and did not find any peculiar behavior.

Long-term fluctuations in the neutron beam intensity (of the order of a ''wheel'' time, which is the time for the complete data taking for all of the samples mounted on the sample wheel) were taken care of by rapidly cycling sample positions, in particular sample-in and sample-out. Beam fluctuations on a time scale too short to be removed by the cycling of sample positions can in principle lead to errors if the resulting fluctuations in dead time are not properly taken into account. If the size of the fluctuations is known, effects of these fluctuations may be corrected by a method developed by Moore [8], who showed that the analytic dead-time correction is altered when fluctuations are taken into account. We have used this method to show that beam fluctuations are not a significant contributor to the uncertainties in the present experiment. Beam fluctuations are characterized by σ/μ, where σ is the standard deviation of the beam intensity and μ the mean beam intensity. Values of σ/μ in this experiment were typically in the 4% range. This number was arrived at by a statistical analysis of the sum of the counts in each time-of-flight spectrum as a function of run number. We also examined the logarithm of the proton beam current on the spallation target on a 1-min time scale, which did not show large fluctuations.

In Fig. 4 we illustrate the very small influence of short-term beam fluctuations in a particularly important case, the measurement of the hydrogen cross section by comparing the transmission of CH_2 and C samples. Figure 4(b) shows the effect of carrying out the correction for beam fluctuations assuming an unrealistically high value of 20% for σ/μ, using the data collected with detector 1. The quantity shown is the percentage difference between the hydrogen cross sections calculated with and without the beam-fluctuation correction. Figure 4(c) shows the same quantity using the data from detector 2. For both detectors the magnitude of the correction is less than 0.8%. Since the actual value of σ/μ is very much smaller than the assumed 20%, we did not make the additional corrections for beam fluctuations.

B. Dead time

Our approach to dealing with dead-time effects was tested by substituting the neutron beam with gamma sources sufficiently intense to yield count rates comparable to those encountered during the actual experiment. Then we recon-
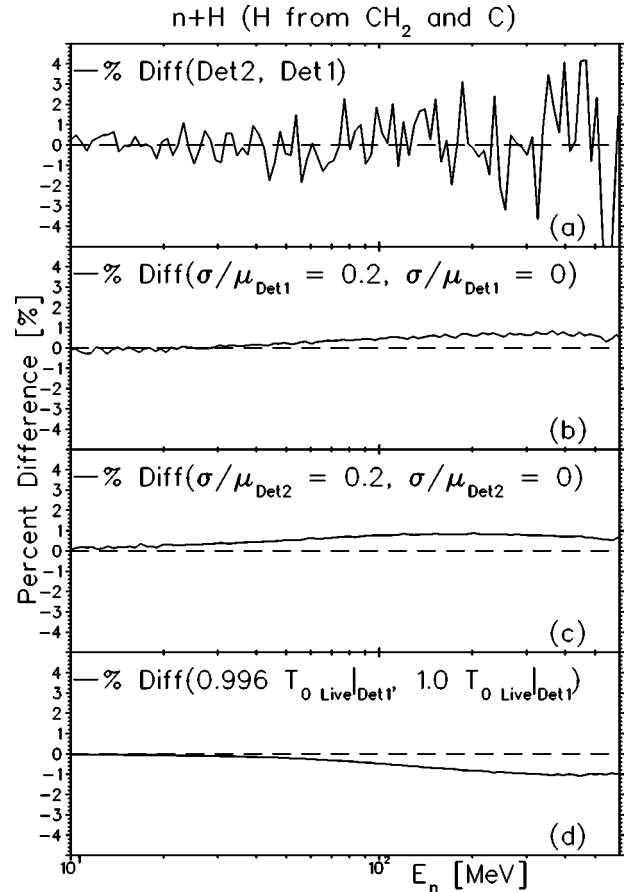

FIG. 4. Sensitivity of the hydrogen total neutron cross section to fluctuations in the beam intensity and in the accuracy of determining live T_0's. The top graph shows the percent difference between cross sections determined from detector 2 and detector 1 as actually calculated, which assumes correct values of $T_{0\ live}$ and no fluctuations in the beam intensity. The next two graphs show the effect of a 20% relative variance in the beam intensity for each of the two detectors; see discussion in Sec. VI A. The bottom graph shows the effect on the cross section from detector 1 if the number of live T_0's were misscaled by 0.4%. The quantity % Diff(a,b) is defined as $200(a-b)/(a+b)$.

structed the gamma spectrum, knowing the number of counts going into the system. Since the gammas arrived at random, we expected a flat distribution after reconstruction. We were able to reproduce the number of counts sent into the system to within less than 1% over a wide range of count rates, with the expected flat distribution.

This exercise led us to the discovery of an error in scaling the $T_{0\ live}$ counts, described further in [7]. This problem affected only data taken with detector 1 in approximately the first half of the experiment and was subsequently corrected. The effect on the data was small ($<0.5\%$) except for very thin samples (such as ^{10}B, ^{11}B, ^{13}C) at energies above 100 MeV where the attenuation is very low. In these cases we relied exclusively on measurements with detector 2, which was unaffected by the problem.

However, the data in Ref. [1] were affected by this problem, since that experiment used virtually the same electronics setup as the present one, although the exact timing might
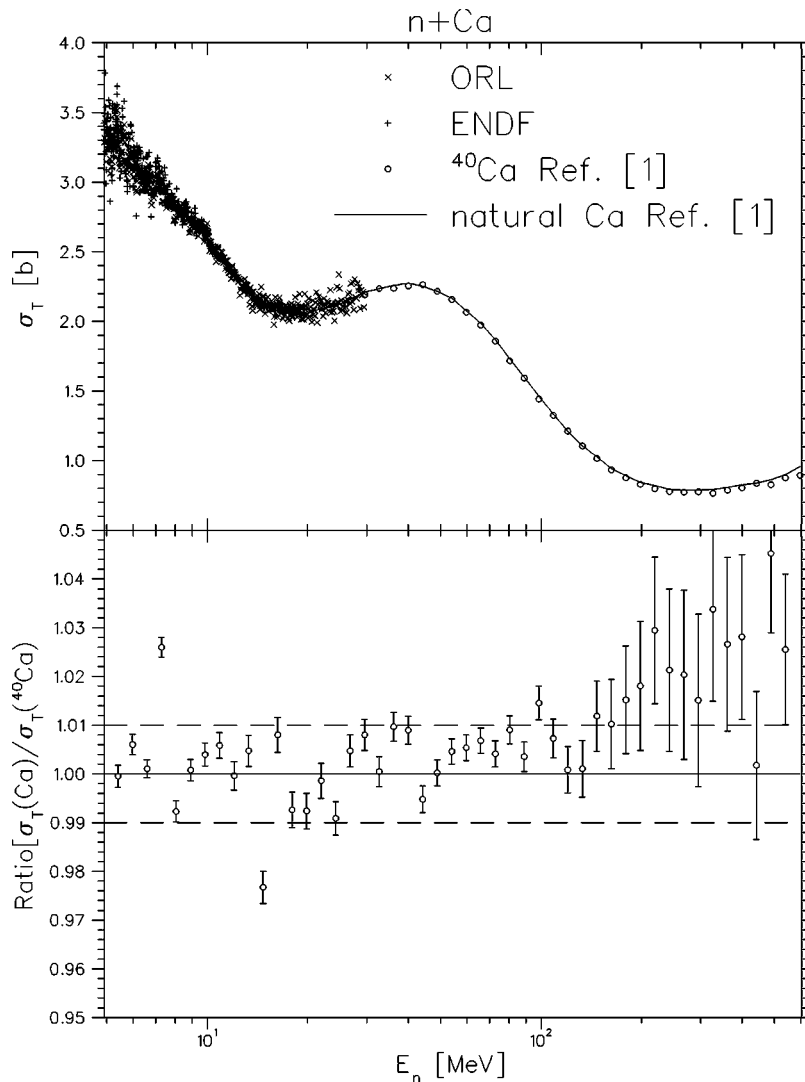
FIG. 5. Upper graph: the total neutron cross section of natural Ca extracted from CaF (Ref. [1]) using the present F cross section, in comparison to an ENDF/B-VI evaluation [9] and a measurement by Perey *et al.* [10]. Lower graph: the cross section ratio of natural Ca to ^{40}Ca in 10% energy bins showing the effect in [1] of the $T_{0\,live}$ scaling problem (see text) above 100 MeV.

have been slightly different. Figure 5 shows a comparison of the ^{40}Ca data taken from Ref. [1] and natural Ca extracted from CaF also measured in Ref. [1], combined with F measured in this experiment. The ratio plot shows the cross section ratio very close to unity below 100 MeV. The higher value (≈ 2.5–3 %) above 100 MeV is attributed to the T_{0live} scaling problem that affects data for thin targets, since the ^{40}Ca sample was the thinnest sample in Ref. [1]. The magnitude and energy dependence of this effect is consistent with what we observed in the present experiment before the correct $T_{0\,live}$ scaling was applied.

We therefore view Fig. 5 as an indication of a systematic error in the ^{40}Ca measurement in Ref. [1], since natural Ca is 97% ^{40}Ca and the cross sections should be nearly identical. The error is largest at energies where the sample attenuation is small, which is why the error is largest in the 200–600 MeV region where the cross section is smallest. Only the C sample in Ref. [1] (see Fig. 6) was thin enough to result in a similarly large systematic error, although all samples in [1] should be somewhat affected.

C. Dependence of cross sections on sample thickness

Measuring cross sections with very thin targets requires careful control of systematic errors associated with sample-

in/sample-out count-rate normalizations, and also requires highly stable beam conditions and electronics. An important check on these errors can be made by comparing cross sections with samples of the same composition but different length, and we made numerous checks of this type during the course of the experiment using carbon, Teflon, and steel samples.

Figure 7 shows the ratio of cross sections using detector 2 for the 2- and 9-cm carbon samples. The attenuations of the two samples at 300 MeV (near the cross section minimum) are approximately 20% for the long carbon sample and 4.7% for the short sample. The latter is comparable to the attenuation of the thinnest sample of interest, ^{11}B, which has an attenuation of about 4.5% at 300 MeV. The slight overall deviation of the ratio from unity (approximately 0.5%) is within the uncertainty of the sample density determinations. There is no evidence for an energy dependence of the ratio beyond the level of about 0.5%.

We also measured the sample-length dependence of our hydrogen cross section measurement, using two different lengths (50 and 25 cm) of high molecular weight CH_2, together with appropriate lengths of carbon compensators. We note that the beam attenuation due to the hydrogen compo-

nent in the shorter CH_2 sample is similar to that from a 2-cm-thick carbon sample in the energy range above 100 MeV. Thus the consistent results shown in Fig. 7 for 2- and 9-cm carbon samples gives us confidence that we can extract an accurate measurement of the H cross section from the measurements on CH_2 and C_8H_{18}, in spite of the small attenuation due to H. Results are shown for the H cross section extracted from the two CH_2 samples, together with those from the C_8H_{18} sample, in Fig. 8. No evidence of systematic differences among these measurements was evident and they have been combined as a weighted average in the final determination of the hydrogen cross section shown in the figure.

D. Detector 1 vs detector 2 consistency

Comparing cross sections determined from the simultaneous measurements with the two detectors is a useful check on systematic errors, since the two detectors have different count rates, different types of discriminators, and different threshold settings. The comparison was excellent except for runs that were disregarded because the error noted above in Sec. VI B in scaling $T_{0\ live}$ for detector 1 led to excessively large ($>0.5\%$) cross section errors. Differences between results with the two detectors beyond those attributable to statistical fluctuations were less than 1%. Examples are shown in Fig. 9 for carbon samples of four lengths ranging from 2 to 15 cm length and in Fig. 4(a) for the hydrogen cross section measured from a CH_2-C comparison.

E. Short-term reproducibility

The reproducibility of a given total neutron cross section was checked by determining the cross sections from subsets of runs of a given "wheel" and plotting the differences. This went as far as analyzing every run of a wheel individually, calculating the weighted average, and then comparing the results to the accumulated total neutron cross section. This was done in the case of the "C-long" sample ($l = 9.012$ cm) with no significant difference. During the running of several "wheels" beam conditions deteriorated rapidly, or beam production was very erratic for short time periods, forcing us to discard a number of runs. Also, during several occasions we had to deal with failures in one or the other detector electronics circuits. Throughout the experiment we kept track of the system performance and stability by monitoring raw scaler ratios and ratios of integral time-of-flight spectra counts to scaler counts.

F. Long-term reproducibility

Throughout the experiment carbon samples of several lengths were remeasured. Comparing the cross sections for a given "wheel" to the ones from previous "wheels" served as a check on whether any aspect of the experiment has changed. Systematic differences were well below 1% for both detectors.

G. Veto accidentals

As noted earlier, the existence of accidental coincidences between the veto paddles and main counters and the conse-quent distortion of the neutron time-of-flight spectrum was understood and corrected for. In many cases the correction is difficult above 560 MeV, and we therefore take 560 MeV as the upper limit for validity of the data except where noted otherwise. In some cases, insufficient data were available to make the correction and the upper limit is taken to be 500 MeV. This effect introduced an extra 1% systematic uncertainty above 520 MeV. This correction was made using singles time-of-flight data for the veto and main counters taken in special runs. The corrections are quite small ($<0.5\%$) except at high energies (>520 MeV) where they can be as large as 10%. The reason for the large correction at the high-energy end of the spectrum is that in this case the intense gamma peak in the main counter falls within the coincidence resolving time between the counters. An example of the correction is shown in Fig. 10 for a run taken with a 9-cm-long carbon sample. Below we show evidence that the cross sections measured in the 1990 runs were similarly distorted by accidental coincidences at high energies.

H. Sample densities

Uncertainties in the areal density of the samples are in several instances the main contributing factor to the systematic uncertainty in the determination of the final total neutron cross sections. As indicated earlier, areal density was determined in as many as three ways: by physical measurements of mass and dimensions, by a bulk density measurement by water immersion coupled with a length measurement, and by gamma-ray attenuation. From the consistency of the measurements with the various techniques and comparison with tabulated densities for solid samples, we estimate that uncertainties in the densities of nearly all of the samples used in this experiment are 0.5% or less. Exceptions are ^{13}C (3.7%), ^{11}B (1.6%), and Mn (1%).

I. Comparison with 1990 runs

We believe the systematic uncertainties in this measurement, apart from those due to areal density determination, to be approximately 1%. Because of a considerable effort to understand and minimize systematic uncertainties in the present measurements, new light has been shed on the results presented in Ref. [1]. Figure 11 shows a comparison between the cross section results of the current measurements and the results in Ref. [1] in the energy region of largest transmission. Adjacent elements are generally in good agreement (better than 1.5%). Notable exceptions are nitrogen, aluminum, ^{90}Zr, and ^{208}Pb. Part of the deviation may have a physics reason. Figure 11 also suggests that the data from the current experiment may be systematically higher by roughly 1.5% than the 1990 experiment. A systematic shift is not indicated in similar plots of the the data from the two experiments below 100 MeV. The possibility of such a shift in the region of low transmission and its absence at lower energies is consistent with the effect associated with $T_{0\ live}$ scaling discussed below.

In addition to possible uncertainties in areal density determination, the remaining differences in the two sets measurements can be attributed to two factors.
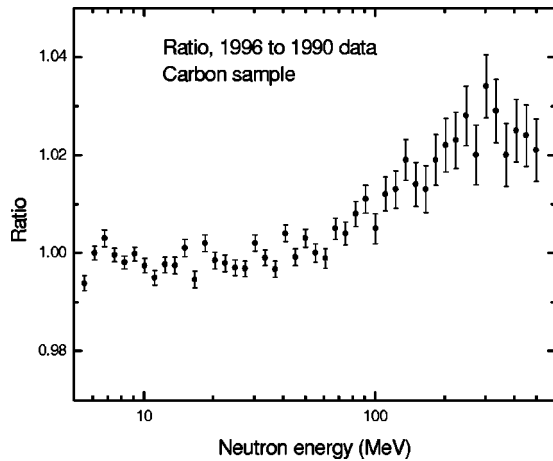
FIG. 6. Ratio of the neutron total cross sections as evaluated in this measurement from the transmission through a 9.012-cm-long ($nl=0.786$ atom/b) C sample to the measurement in Ref. [1]. The C sample in Ref. [1] was 9.261 cm long ($nl=1.0448$ atom/b). Above 100 MeV one can clearly see the effect of miscounting the number of $T_{0\,live}$ in the 1990 measurement.

Veto correction. Figure 12 shows the neutron total cross sections above 250 MeV of the Sn and Bi cross sections measured in Ref. [1], compared with nearby samples (In and Pb) measured in the present work. Above approximately 530 MeV one can see an anomaly in the earlier cross sections which we ascribe to the same veto accidental coincidence problem discussed in Sec. VI G. The anomaly resembles that in the uncorrected (dotted) curve shown in Fig. 10, although the effect is smaller in the 1990 runs because the gamma peak was more strongly attenuated in that experiment. Accordingly, we recommend that data above 530 MeV taken in the earlier experiment be disregarded.

$T_{0\,live}$ *scaling.* As described in [7] and Sec. VI B, a slight misscaling of the number of $T_{0\,live}$'s was discovered and corrected during the experiment described here. This error
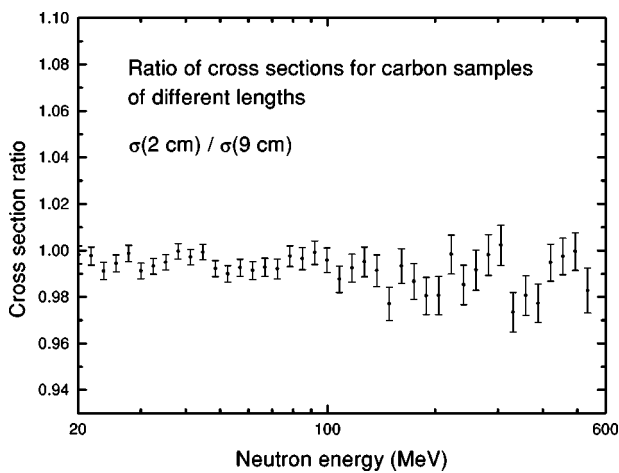
FIG. 7. The detector 2 cross section ratio for the 2- and 9-cm carbon samples. The results were binned in 8% bins in order to achieve adequate statistical accuracy. This figure shows no systematic differences between the two cross section determinations beyond an amount attributable to sample density determination.
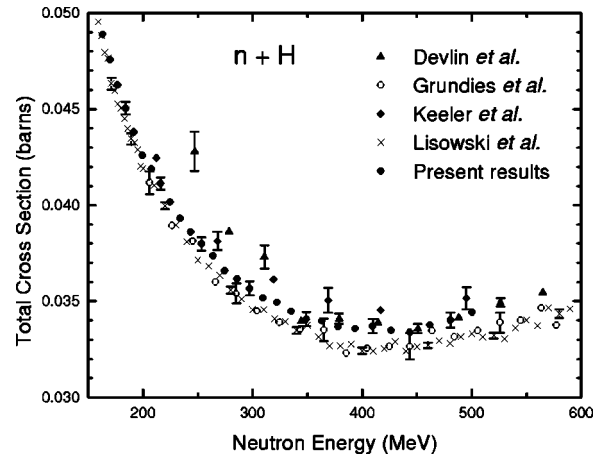

FIG. 8. Results are shown for the H cross section extracted from the two CH_2 samples combined with those from the C_8H_{18} sample.

was present in the 1990 runs. The consequence of this problem is a downshift of the calculated cross section in a manner that is energy dependent because of the way the number of $T_{0\,live}$'s enters the analytic dead-time correction and because the effect is highly dependent on sample transmission. The effect is only important above approximately 100 MeV as can be seen from Figs. 5 and 6. We therefore recommend a systematic uncertainty of 3% for the ^{40}Ca measurement, 2%

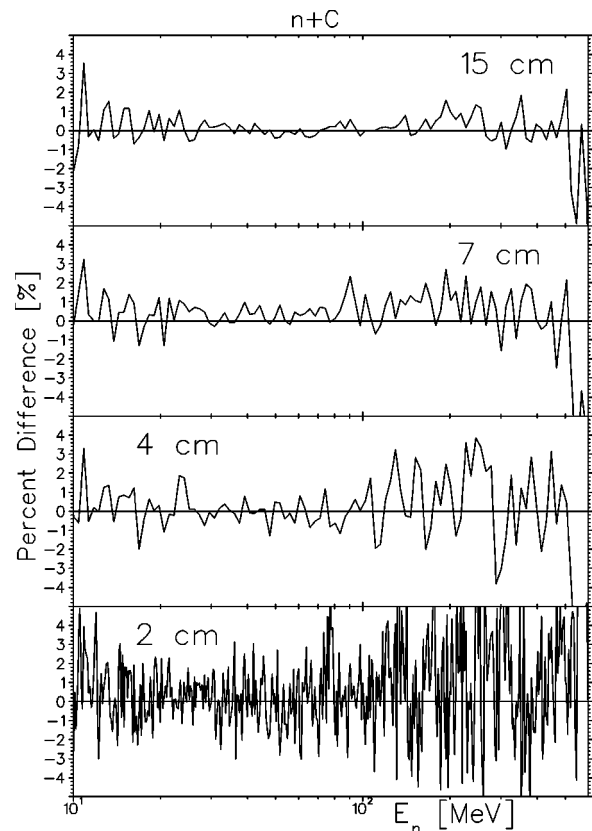
FIG. 9. Detector 1 and detector 2 differences for carbon samples of several lengths. The percent difference (% Diff) is calculated as follows: % Diff$=200(\sigma_{Det2}-\sigma_{Det1})/(\sigma_{Det2}+\sigma_{Det1})$.
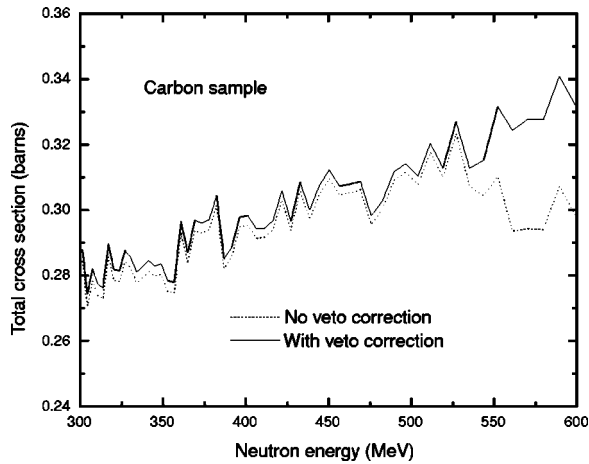
FIG. 10. Cross sections from one of the runs on the 9-cm-long carbon sample before and after applying the correction for accidental coincidences in the veto counter. Results are shown for detector 1; those for detector 2 are similar.

for the C measurement, and 1.5% for the remaining cross sections above 100 MeV in Ref. [1].

VII. SPECIAL CONSIDERATIONS FOR H AND D

The hydrogen total cross section was determined by measuring the transmission of liquid (octane, C_8H_{18}) and solid (polyethylene, CH_2) samples relative to the transmission of carbon (graphite) samples. The octane sample was approximately 62 cm long, and the two polyethylene samples were approximately 50 and 25 cm long. The lengths of the carbon compensating samples were chosen so that the areal density of carbon nuclei was very nearly the same as for the corresponding hydrogenous samples. The deuterium-hydrogen cross section difference (D-H) was determined by measuring the relative transmission of light and heavy water samples of closely matched lengths, approximately 50 cm. All liquid
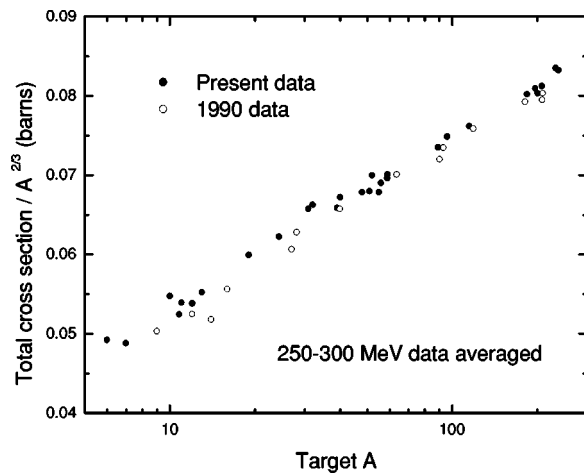

FIG. 11. Comparison between the cross section results (scaled by $A^{2/3}$) of this measurement and the results in Ref. [1] as a function of A in the energy region of largest transmission. The data shown are the cross sections averaged over the 250–300 MeV energy range.
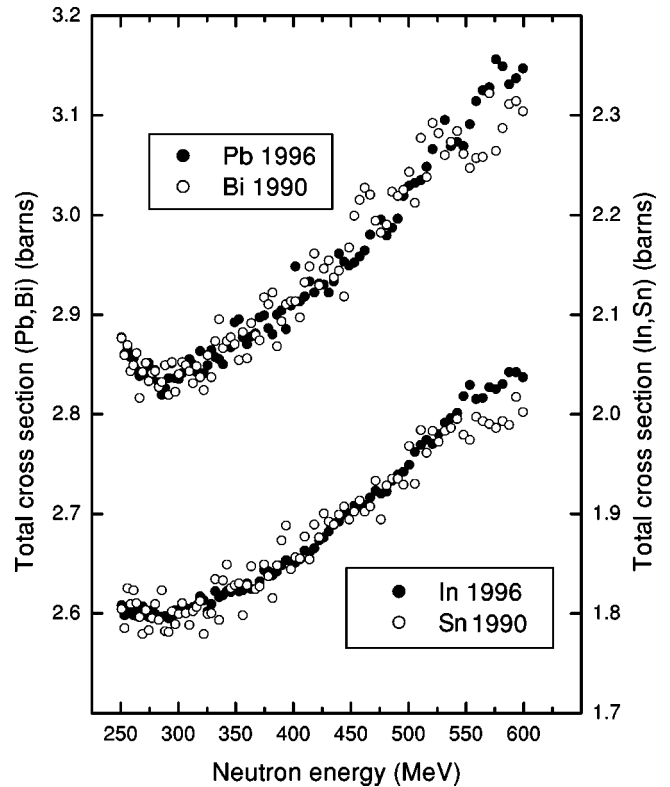

FIG. 12. Total cross sections for Bi and Sn from the 1990 runs [1] compared with the neighboring samples Pb and In from the current experiment. The 1990 results were normalized to the corresponding 1996 cross sections in the 250–300 MeV range to facilitate comparison of the shapes of the cross sections at higher energies. The cross sections in the 1990 runs are too low above approximately 530 MeV because of neglect of accidental coincidences between the veto and main detectors.

samples were contained in aluminum cylinders of 3.175 cm inside diameter, which was significantly larger than the size of the collimated neutron beam and also sufficient for inclusion of an air bubble to allow for expansion and contraction of the liquids. The aluminum endcaps were carefully measured to ensure uniformity, and for the hydrogen measurements using the octane sample a pair of endcaps was affixed to the carbon compensating sample. Tables II and III summarize the main characteristics of the liquid and solid hydrogen and deuterium compounds used in this experiment.

For the H and D-H measurements, two samples were mounted on the sample wheel. For the H measurements, these were one of the hydrocarbon samples (octane or polyethylene) and the corresponding carbon compensator. For the D-H measurements, they were the light and heavy water samples. In running the experiment the sample wheel alternated between these two positions. Because these measurements did not require an open-beam measurement, count rates were lower than in the remainder of the measurements described in this paper. Therefore, the polyethylene beam attenuator upstream of the samples was removed for all of the H and D-H cross section measurements, with the exception of that for the 25-cm-long polyethylene sample.

Both liquid and solid compounds were used for the H

measurements because of concerns that the C and H concentrations might vary from the 1:2 stoichiometric ratio in polyethylene. This problem is minimized for high-molecular-weight polyethylene, and accordingly we acquired a 50 cm length of high-molecular-weight polyethylene from Poly Hi Solidur with a nominal purity of better than 99.9%. As a check of the uniformity of the sample we cut the 50-cm polyethylene sample in half and repeated the measurement with shorter sample and corresponding carbon compensator; this is the 25-cm sample referred to above. The density of the octane sample varied significantly with temperature, which was monitored and taken into account in the analysis. As a check of the consistency of this procedure the data were divided into two temperature regions; the cross sections extracted from the two data sets showed no apparent differences. Small corrections using known C total neutron cross sections from Ref. [1] were necessary because of a slight mismatch of areal densities in the samples whose transmission was being compared, but this correction incurred negligible systematic error ($<0.1\%$).

There was no evidence for errors beyond statistical uncertainties in the hydrogen total cross sections extracted from the octane sample and the two lengths of polyethylene sample. It should also be noted that each sample required a different length of carbon compensator, and the excellent agreement among the results suggests that there were no peculiarities in the internal structure of the graphite compensators, such as voids, that might upset the compensation.

We are confident that we have measured the small differences in attenuation between the hydrogenous samples and their carbon compensators accurately. The attenuation near 300 MeV due to the hydrogen within the octane and long polyethylene samples is approximately twice that of the 2-cm-long C-short sample, and according to Fig. 7 in Sec. VI we were able to measure the carbon cross section for this short sample well within systematic uncertainties at or below the 1% level. This conclusion is also supported by the consistency of the results obtained with the full- and half-length polyethylene samples.

For the D-H cross section difference measurement it was particularly important to characterize the sample composition and areal density very accurately, since an error of 0.1% in the relative areal densities of the light and heavy water samples propagates into an error of the order of 1% in the final result over a portion of the energy range. Careful measurement of the lengths of the sample tubes ensured that the sample lengths were known to approximately 0.03%. Deionized water with naturally occurring abundances of hydrogen isotopes was used for the light water sample. The heavy water sample was commercially available D_2O with enrichment greater than 99.9%. Just before filling the cans, the water samples were pumped to remove dissolved gases. All results were corrected for density variations with temperature. The total cross section of oxygen measured in [1] was used to make a correction for the difference in the areal densities of the oxygen nuclei between the two samples; this correction was small enough to yield a negligible systematic error in the D-H cross section result [11].
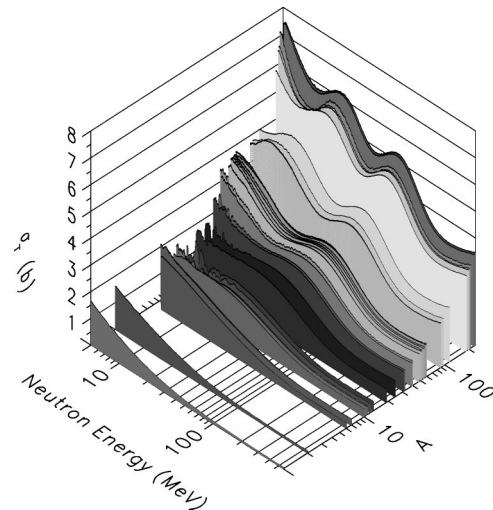

FIG. 13. Results for 31 of the 37 samples measured. Not shown are the results for the separated isotopes ^{54,56}Fe and ^{182,183,184,186}W.

VIII. RESULTS

Figures 13–15 depict a sampling across the periodic table of the total neutron cross sections measured in this experiment compared to previous measurements. The comparison data sets are by no means complete: only a few are shown. Besides being representative, samples were chosen according to the availability of previous data sets covering a wide energy range. There is generally excellent agreement between the data sets.

Compound resonances arising from the interference of many nearby states can be seen in the cross sections of the lighter elements such as Mg, S, and P, whose analysis allows the extraction of level density information. The large-scale structure seen in the cross sections of the medium and heavier elements is the result of potential scattering, which gives rise to interferences between the incident wave function and the wave transmitted through the nuclear potential. This broad structure is reproduced by a simple parametrization of the data based on a Ramsauer-effect model [2,3]. The results for the total cross section difference deuterium-hydrogen (D-H) have been used to test the Faddeev description of the $n+D$ total cross section between 10 and 300 MeV [5].

The data will be made available from the National Nuclear Data Center at the Brookhaven National Laboratory in 1% energy bins. However, the energy resolution is significantly better than this at low energies, and data without such binning will be supplied on request by the authors.

IX. OPTICAL-MODEL INTERPRETATION

We have tested two types of microscopic folding-model optical-model calculations. The energy range encompassed by these models is roughly 10–600 MeV and the mass range extends from the lithium isotopes through uranium. Microscopic formulations of the optical model have very few free parameters and are intended as a complement to the development of a phenomenological global optical model up to 2
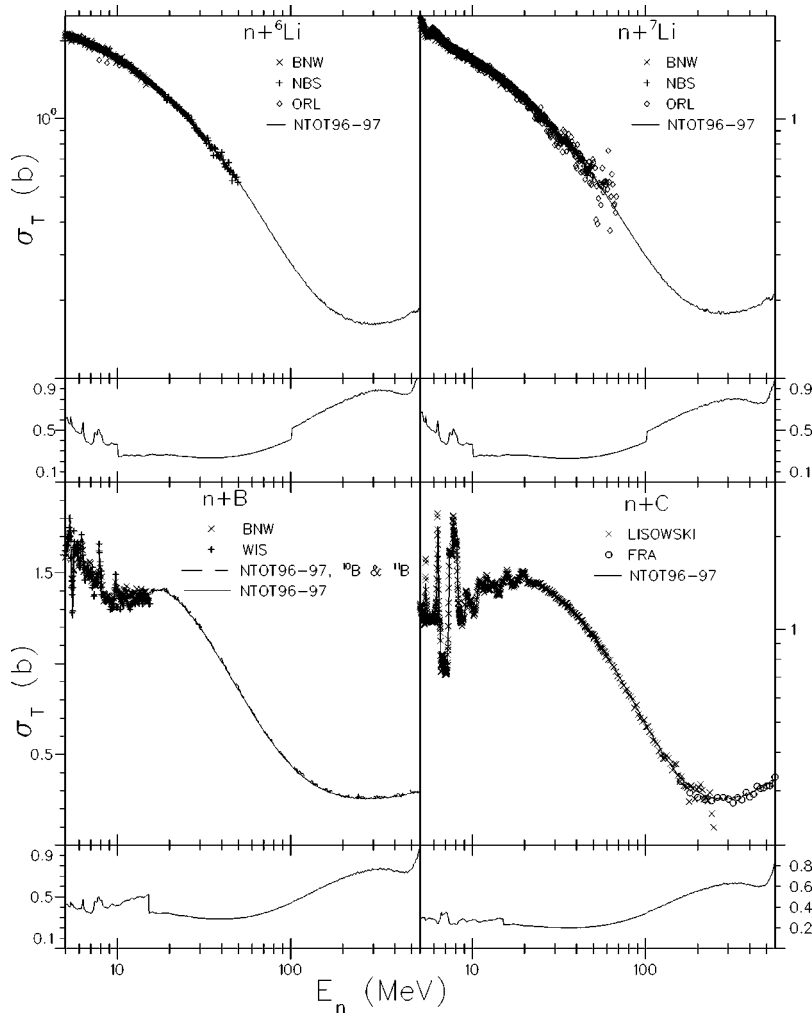
FIG. 14. Upper left: the total neutron cross section of ^{6}Li compared to measurements by Foster and Glasgow [12], Lamaze *et al.* [13], and Harvey and Hill [14]. Upper right: the total neutron cross section of ^{7}Li compared to measurements by Foster and Glasgow [12], Lamaze *et al.* [13], and Harvey and Hill [15]. Lower left: the total neutron cross section of B compared to measurements by Foster and Glasgow [12] and Fossan *et al.* [16]. Also shown is a comparison to the composite cross section of ^{10}B and ^{11}B, combined according to their natural abundances. Lower right: the total neutron cross section of natural C compared to measurements by Lisowski *et al.* [17] and Franz *et al.* [18]. The present data, indicated as NTOT96–97, are shown in 1%-wide energy bins. Statistical uncertainties in the present data are shown below each cross section graph in percent; these also refer to data in 1%-wide energy bins. The sharp edges in the uncertainties in the 10–20 MeV region result from the way detector 1 and detector 2 data sets are combined.

GeV being undertaken by Madland and Sierk [24]. The results reported here will be used in improving the quality of the nuclear cross sections in the MCNPX code system and associated data libraries.

The results of the neutron total cross section measurements described above, when taken together with the 1990 measurements [1], provide an extensive database for the testing and refinement of optical models. The earlier measurements have already proved useful for such tests, and a study by Finlay and Feldman [25] using those data has shown that few existing formulations of the optical potential, either relativistic or nonrelativistic, have sufficient predictive capability to describe total cross sections adequately. The recent set of measurements has significantly extended the total cross section data base for light nuclei, which are very difficult to fit using standard multiparameter regional optical models with Woods-Saxon form factors.

In this paper we show calculations using two variants of the microscopic folding model for the optical potential. These are the Jeukenne-Lejeune-Mahaux (JLM) potential [26–28], based on many-body calculations of the optical potential in infinite nuclear matter, and the empirical effective interaction (EEI) approach of Kelly and Wallace and collaborators ([29] and references therein). In applying both of these approaches, an energy- and density-dependent effective nucleon-nucleon interaction is convoluted with the nuclear density to yield the optical potential. This procedure minimizes the number of free parameters, and is particularly advantageous for light nuclei, since the rapid variation of nuclear shapes from nucleus to nucleus in this mass region is largely taken into account by the use of realistic densities. Moreover, the Finlay-Feldman study [25] indicated that these two approaches show promise in addressing neutron total cross section data over a large fraction of the energy range being investigated.

It is hoped that an optical model that reproduces total cross sections well will then predict reliable values for reaction cross sections. Experimental data on neutron reaction cross sections are sparse and insufficiently accurate to test this possibility. However, the database for proton reaction cross sections is much more extensive, and an optical model that reproduces neutron total cross sections should reproduce these data if the isovector terms are well characterized. Accordingly, we have calculated proton reaction cross sections using the EEI-based optical model and compared it with a set of measurements [30] available in the energy range where the EEI is applicable (135–650 MeV). It will be seen below that this comparison is successful, which suggests that the EEI-based model may also be useful for the prediction of neutron reaction cross sections.
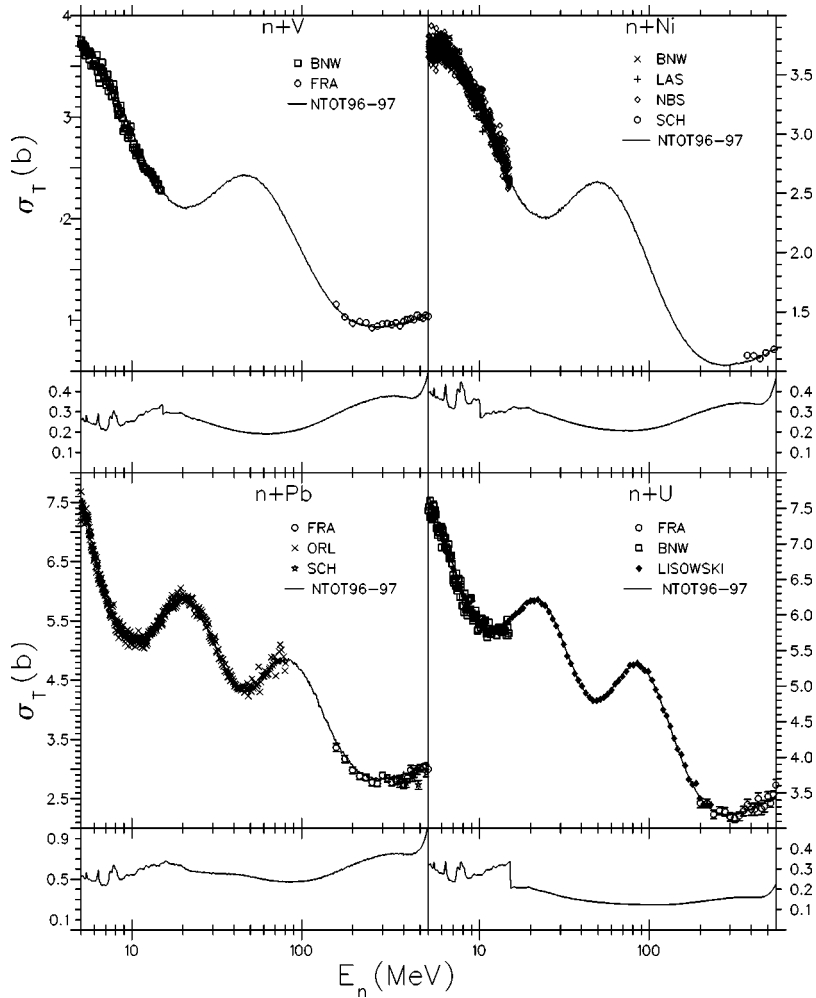
FIG. 15. Upper left: the total neutron cross section of natural vanadium compared to measurements by Foster and Glasgow [12] and Franz et al. [18]. Upper right: the total neutron cross section of nickel compared to measurements by Foster et al. [12], Nereson and Darden [19], Schwartz et al. [20], and Schimmerling et al. [21]. Lower left: the total neutron cross section of natural lead compared to measurements by Franz et al. [18], Larson et al. [22], and Schimmerling et al. [21]. Lower right: the total neutron cross section of ^{238}U compared to measurements by Foster and Glasgow [12], Franz et al. [18], and Lisowski [23]. The present data, indicated as NTOT96–97, are shown in 1%-wide energy bins. Statistical uncertainties in the present data are shown below each cross section graph in percent; these also refer to data in 1%-wide energy bins. The discontinuities in the uncertainties result from the way detector 1 and detector 2 data sets are combined. Only detector 1 data were available for the Pb measurement.

A. Densities

The folding-model calculations reported here require both proton and neutron densities. Charge densities were taken from electron-scattering results, as indicated in Table IV. For the most part these were chosen from the compilation of de Vries et al. [31]. Point-proton densities were then obtained by removing the finite size of the proton charge distribution

TABLE IV. Charge densities used in the folding model calculations, taken from the compilation of Ref. [31] except where indicated. Notation is described in Ref. [31].

Nucleus	Source	Nucleus	Source	Nucleus	Source
^{6}Li	MHO	^{16}O	3pF	^{72}Ge	2pF
^{7}Li	HO	^{19}F	First 2pF	^{89}Y	3pG
^{9}Be	First HO	^{24}Mg	First 3pF	^{115}In	2pF
^{10}B	HO	^{27}Al	First 2pF	^{118}Sn	3pG
^{11}B	HO	^{40}Ca	a	^{184}W	2pF
^{12}C	b	^{56}Fe	3pG	^{208}Pb	c
^{13}C	MHO	^{59}Co	Second 2pF	^{238}U	Second 2pF
^{14}N	3pF	^{63}Cu	3pG		

aModified 3pF from Ref. [37].
bSum of Gaussians from Ref. [38].
cSum of Gaussians from Ref. [33].

by deconvolution. These isotopic densities were used for comparison with experimental total and reaction cross section results on both monoisotopic samples and natural samples containing several isotopes. Calculations using phenomenological optical potentials indicate that the errors incurred by using a single isotopic density for polyisotopic samples are significantly smaller than the typical deviation between calculation and experiment. An exception is the calculation of the proton reaction cross section on natural B, for which we used an appropriately weighted combination of ^{10}B and ^{11}B. For ^{63}Cu and lighter nuclei, the point-neutron distribution was obtained by simple scaling by N/Z. For nuclei heavier than ^{63}Cu, allowance was made for a slight increase of the neutron rms radius relative to that for protons as suggested by Hartree-Fock and other types of calculations [32]. Except for ^{208}Pb, this was accomplished by a simple radial scaling $\rho_n(r) = a^3(N/Z)\rho_p(r/a)$. The parameter a, the ratio of neutron to proton rms radii, was taken as 1.02. For ^{208}Pb, the proton density was taken from a model-independent analysis of electron scattering [33], while the neutron density was inferred from a proton scattering experiment [34]; the ratio of neutron to proton rms radii is 1.027. These densities have been used to show that a consistent folding-model treatment of elastic neutron and proton scattering on ^{208}Pb requires an extended neutron distribution [35].

As an alternative, densities for both protons and neutrons may be obtained from an entirely theoretical treatment, such as the Hartree-Fock-Bogoliubov calculations employed in the study of the JLM folding model in Ref. [36]. Since calculations of this type are not available for most of the nuclei investigated in the present work, we rely on the reasonable but cruder estimates of neutron densities described above.

Although some of the nuclei in the present study are known to be statically deformed, particularly ^{238}U and many of the light nuclei, we have employed a spherical optical model. Effects of deformation are partly accounted for by the use of densities determined from electron scattering, since these densities represent the monopole component of the complete deformed charge distributions. The results obtained below do not indicate a clear need for a more detailed treatment of deformation for total and reaction cross sections in the 5–600 MeV energy range.

B. JLM potential

The JLM potential has been rather successful in reproducing a wide variety of nucleon scattering observables. However, there are small but significant differences in details of its application by various authors. A systematic study of this potential up to approximately 65 MeV using a common set of assumptions was carried out by a Livermore/Ohio University/Florida State University collaboration, referred to henceforth as LOF. Some of the results of this work, together with details of the implementation, may be found in Refs. [39–43]. In particular, the model successfully reproduced nucleon scattering from light nuclei in the range $12 \leqslant A \leqslant 27$ [40]. More recently, a thorough study of the JLM approach extended up to 200 MeV for $A \geqslant 40$ has been reported [36] by a group at Bruyères-le-Châtel; this study will be referred to as B3.

The optical potential may be written in the form

$$U_{opt} = U_{cen} + \boldsymbol{l} \cdot \boldsymbol{\sigma} U_{so}, \tag{9.1}$$

where U_{cen} and U_{so} are complex functions with signs defined so that the real part of U_{cen} is negative for an attractive potential. In comparing calculations with experimental data, both the LOF and B3 studies optimized the agreement by adjusting normalizing parameters λ_v and λ_w in the expression for the central potential,

$$U_{cen} = \lambda_v V_{cen} + \lambda_w W_{cen}, \tag{9.2}$$

in which V_{cen} and W_{cen} are the real and imaginary parts of the potential calculated from the JLM model. Both LOF and B3 studies yield values of λ_v in the range approximately 0.95–1.0. For λ_w, values in the range 0.8–0.9 were typical in the LOF study, whereas in the B3 study the values are approximately 1.2 from 10 to 100 MeV, with a pronounced rise at higher energies. The difference between the two studies is a consequence of the prescription for applying the local density approximation in the JLM model; LOF evaluated the density at a point midway between target and projectile nucleons, whereas B3 used the target-nucleon position. In the present work we adopt the LOF prescription, since this

yields a surface peak in the imaginary potential at low energies that is in reasonable agreement with phenomenological potentials. In contrast, the target-nucleon prescription yields an imaginary potential with a shape that differs significantly from the phenomenological one, as shown in [39]. To make a clear test of the JLM model we have chosen to keep both of the normalization parameters constant across the energy range 5–160 MeV; the upper limit in the present calculations corresponds to the upper end of the range of applicability as stated by JLM [26–28]. We have used the original parametrization of the JLM potential in [26–28] and have not employed the reparametrization for low energies proposed in [44]. An additional small difference between the implementations in the LOF and B3 studies is the size parameter t in a Gaussian smearing function that represents the range of the effective nucleon-nucleon force (see, e.g., [39]). This parameter was taken as $t = 1.0$ fm in the LOF study, whereas a somewhat larger value (1.2–1.3 fm) was found more appropriate for a global fit for $A \geqslant 40$ in the B3 work. The sensitivity of the results to this parameter will be discussed further below (see, in particular, Fig. 18).

It is well known that scattering in the medium-energy range requires a complex spin orbit interaction. Following its successful use in the B3 study, we supplement the JLM central potential with a simple zero-range form for the spin-orbit potential as proposed by Scheerbaum [45],

$$U_{so} = \frac{\hbar^2}{2m^2 c^2} (\lambda_{vso} + i\lambda_{wso}) \frac{1}{r} \frac{d}{dr} \left[\frac{3+\tau}{6} \rho_p + \frac{3-\tau}{6} \rho_n \right], \tag{9.3}$$

where τ is $+1$ for incident neutrons and -1 for protons. The quantities ρ_p and ρ_n are the point-nucleon densities for protons and neutrons, respectively. We employ the values determined in the B3 study [36] for the real and imaginary strength parameters λ_{vso} and λ_{wso},

$$\lambda_{vso} = 130e^{-0.013E} + 40 \text{ MeV fm}^3, \tag{9.4}$$

$$\lambda_{wso} = -0.2(E - 20) \text{ MeV fm}^3, \tag{9.5}$$

where E is the laboratory incident energy in MeV.

Results of the JLM calculations are compared with the total cross section data in Figs. 16–18. Figure 16 shows results for nuclei in the range ^{6}Li–^{59}Co using parameters $\lambda_v = 1.0$, $\lambda_w = 0.8$, and a range parameter 1.0 fm, which are consistent with the light nucleus study of Ref. [40]. The heavy nuclei are better reproduced with somewhat different parameters $\lambda_v = 0.95$, $\lambda_w = 0.8$, and range parameter 1.2 fm, as shown in Fig. 17 for a selection of nuclei in the range ^{59}Co–^{238}U.

The effects of altering λ_v and the range parameter t are indicated for ^{59}Co in Fig. 18. This figure shows that increasing the range parameter from 1.0 to 1.2 fm results in an increase in the total cross section without a significant change in its energy dependence. On the other hand, increasing λ_v from 0.95 to 1.0 moves the maxima and minima of the cross section to higher energies with very little change in magnitude. The behavior of the cross sections in Fig. 17
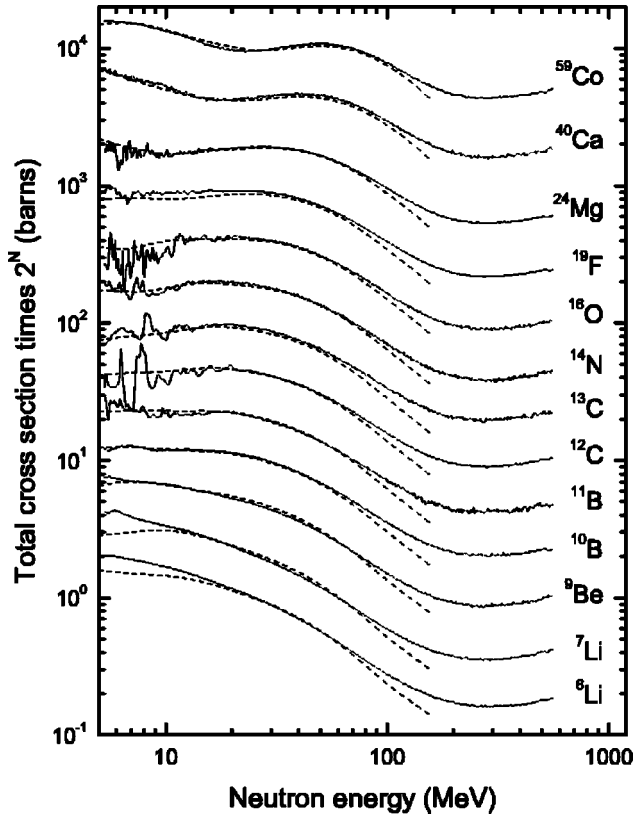
FIG. 16. The dashed lines show calculations of neutron total cross sections using the JLM potential for the indicated isotopes, with $\lambda_v = 1.0$, $\lambda_w = 0.8$, and range parameter 1.0 fm (see text). The data are from a combination of the 1996 and 1990 LANSCE/WNR runs [7,1] and employed natural samples except for the separated isotopes ^{6,7}Li, ^{10,11}B, and ^{13}C. The scaling exponent N (see ordinate label) is 0 for ^{6}Li and increases by 1 for each higher nucleus.

FIG. 17. The dashed lines show calculations of neutron total cross sections using the JLM potential, with $\lambda_v = 0.95$, $\lambda_w = 0.8$, and range parameter 1.2 fm (see text). The data on natural samples are from the 1996 LANSCE/WNR run [7]; the calculations were made for the indicated isotopes. The scaling exponent N (see ordinate label) is 0 for ^{59}Co and increases by 1 for each higher nucleus.

suggests that an even smaller value of λ_v than 0.95 may be appropriate for the largest masses.

We conclude that the JLM model as implemented here provides a reasonable description of total neutron cross sections for energies up to about 80 MeV. This is particularly true for the light nuclei (Fig. 16), whose cross sections appear to be well reproduced above the region where structure is prominent. Above 80 MeV the cross sections drop off rapidly in comparison with the data unless the magnitude of the imaginary potential is significantly increased above the values given by JLM, as was done in the B3 study [36]. Analysis of total cross section data across the broad mass range included in the present analysis suggests a slight but significant A dependence of the parameters used to implement the JLM potential, particularly the real central potential normalization λ_v and the range parameter t.

The overall agreement with the data is less satisfactory for the heavy nuclei (Fig. 17) than for the light nuclei (Fig. 16). This was noticed by Finlay and Feldman [25] who ascribed the deficiency to an inadequacy in the isovector part of the JLM potential. An additional possibility is a deficiency in the density dependence of the potential, since the surface-to-volume ratio is much greater for the light than for the heavy nuclei.
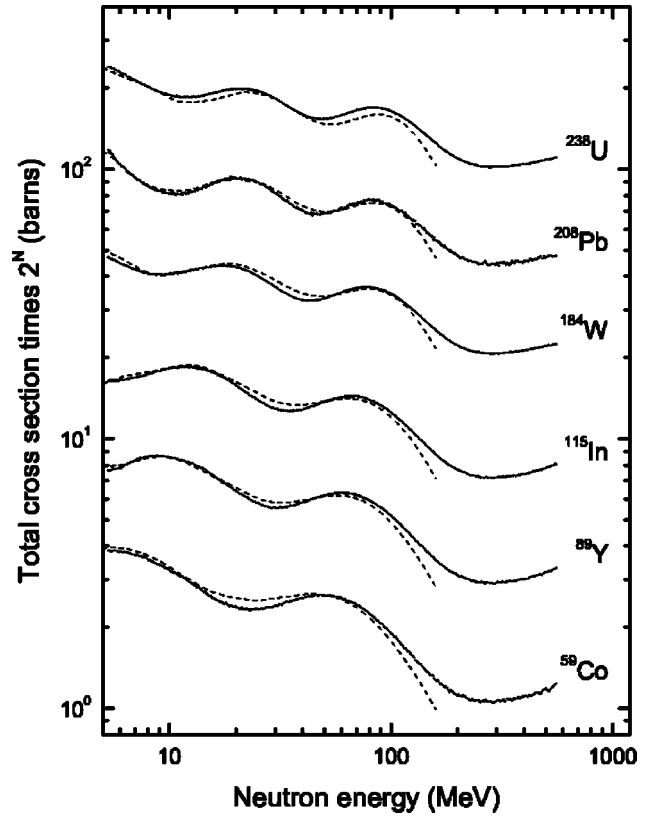
C. Empirical effective interaction

In this section we describe calculations of both neutron total and proton reaction cross sections that have been carried out using a folding model based on the impulse approximation with empirically determined density-dependent corrections. The starting point in this treatment is the free nucleon-nucleon interaction or t matrix of Franey and Love [46]. It is well established that medium corrections to the free nucleon-nucleon interaction must be applied in the energy range of interest here. One approach is to determine the required density-dependent modifications to the free interaction by fitting suitable functional forms for the density dependence to a wide body of scattering data, and such a program has been carried out by Kelly and Wallace and collaborators (see [29] and references therein).

The components of the interaction that Kelly and Wallace chose to modify were the real and imaginary parts of the central isoscalar spin-independent interaction ($\mathrm{Re}\, t_{00}^C$, $\mathrm{Im}\, t_{00}^C$) and the real isoscalar spin orbit interaction ($\mathrm{Re}\, t'^{LS}_0$). The density dependence is expressed via the dimensionless scaled local Fermi momentum κ_F, where $\kappa_F = k_F/(1.33$ fm^{-1}). As indicated in [29], the modified interaction components in momentum space are

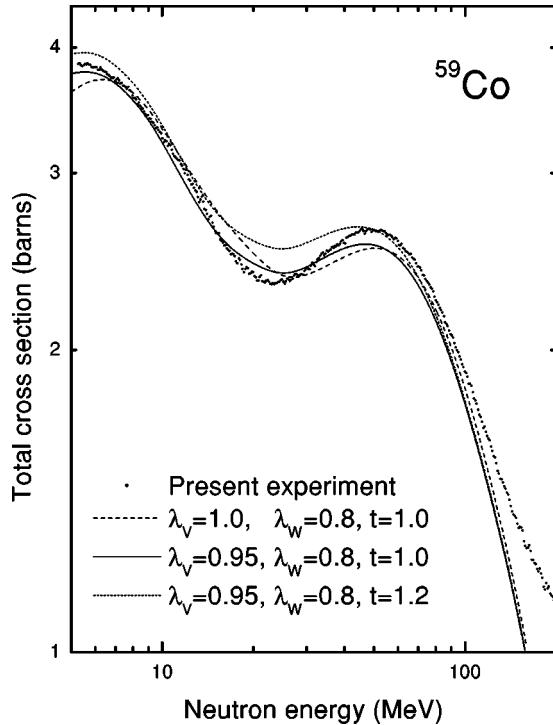$$\mathrm{Re}\, t_{00}^C(q,\kappa_F) = S_1\ \mathrm{Re}\, t_{00}^{C(f)}(q) + b_1 \kappa_F^3 y(q/\mu_1), \quad (9.6)$$

FIG. 18. Calculations using the JLM potential for the total neutron cross section of ^{59}Co, showing the effects of varying the real-potential-strength parameter λ_v and the range parameter t; see text. Data are from the 1996 LANSCE/WNR run [7].

$$\text{Im } t^C_{00}(q, \kappa_F) = [S_2 - d_2 \kappa_F^2] \text{Im } t^{C(f)}_{00}(q), \qquad (9.7)$$

$$\text{Re } t'^{LS}_0(q, \kappa_F) = S_3 \text{ Re } t'^{LS(f)}_0(q) + b_3 \kappa_F^3 y^2(q/\mu_3), \qquad (9.8)$$

where q is the momentum transfer, y is a form factor defined as $y(x) = (1 + x^2)^{-1}$, and the quantities describing the density dependence are the strength parameters S_1, b_1, S_2, d_2, S_3, b_3, and the ranges μ_1, μ_3. The superscript (f) on the right-hand side of these expressions indicates the free nucleon-nucleon interaction, which is the Franey-Love t matrix in the work described here.

The results of fitting the strength parameters (along with reasonable choices for the range parameters) to a wide variety of elastic and inelastic proton-scattering measurements in $T = 0$ light nuclei are shown in Table II of Ref. [29]. The work was carried out at six discrete energies: 135, 180, 200, 318, 500, and 650 MeV. Even though developed for isoscalar light nuclei, this interaction leads to a reasonable reproduction of the total neutron cross sections for both light and heavy nuclei at the energies for which the interaction is available, as shown by Finlay and Feldman [25].

In Fig. 19 we show similar calculations for light, medium-weight, and heavy nuclei (natural C, Co, and Pb) as determined in the measurements described in this paper. The optical potentials used to perform these calculations were generated by a modified version of the ALLWRLD computer code [47] (see also [48]) that allows for the parametrization of the effective interaction as shown above. The Franey-Love t matrix was linearly interpolated between its tabulated energies. The densities employed were those indicated in
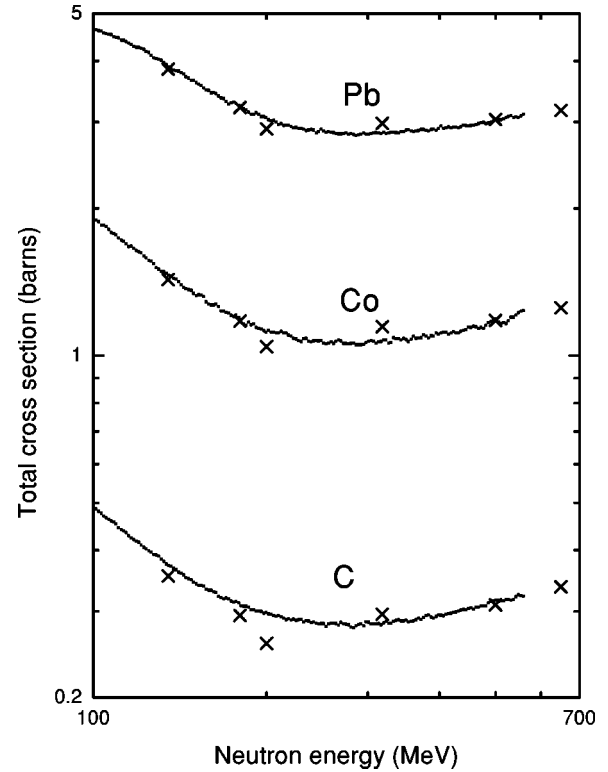

FIG. 19. Neutron total cross sections calculated for ^{12}C, ^{59}Co, and ^{208}Pb using the EEI parametrized at six energies as indicated in [29]. Experimental data (on natural samples) are from the 1996–1997 LANSCE/WNR measurements [7].

Table IV. The calculations were carried out using the zero-range exchange approximation (ZREA), the Slater exchange approximation (SEA) for the mixed densities, and with the use of the self-consistent wave number (SCWN). The optical potential was used in a standard optical model code with relativistic kinematics [49] to calculate observables. It should be noted that the average agreement between calculation and experiment is quite good. Although not shown here (but see [25]), calculations with the unmodified Franey-Love interaction significantly overpredict the data in the energy range below 500 MeV; in the energy region near 200 MeV this overprediction is in the neighborhood of 20%. The medium modifications introduced by Kelly and Wallace are thus seen to be crucial in obtaining the correct behavior of the cross sections. Good agreement is obtained for heavy as well as light nuclei, even though density-dependent modifications were introduced only in the isoscalar part of the interaction. This implies that the unmodified isovector components in the Franey-Love t matrix are adequate for the description of total neutron cross sections and, as will be seen below, for proton reaction cross sections as well. These conclusions are in good agreement with the results of Kelly [50], who studied transparency in $(e, e'p)$ reactions in the context of optical-model and Glauber calculations. In that work Kelly showed that the EEI (and a related relativistic interaction known as IA2) gave a considerably better description of nuclear transparency for intermediate-energy nucleons than could be obtained for several other phenomenological optical potentials from the literature.

TABLE V. Parameters of the empirical effective interaction (EEI) represented as a quadratic function of incident nucleon energy E as discussed in the text. Each of the parameters in the first column is expressed as $Y = c_0 + c_1 x + c_2 x^2$, where $x = (E - 375 \text{ MeV})/(375 \text{ MeV})$. As in [29], the range parameters are $\mu_1 = 1.5$ fm^{-1} for $E \leq 200$ MeV, $\mu_1 = 2.0$ fm^{-1} for $E > 200$ MeV, and $\mu_3 = 6.0$ fm^{-1} for all energies. This parametrization is to be used with the Franey-Love t matrix [46] as the free interaction.

	c_0	c_1	c_2
S_1	1.07	0.2591	-0.1116
b_1	135.0	92.05	-51.14
S_2	0.98	0.075	-0.2510
d_2	-0.1	-0.4705	0.4184
S_3	0.8205	-0.0543	-0.1493
b_3	5.86	0	0

Since the EEI parameters were determined independently at the six chosen energies, it is not surprising that there is a certain amount of scatter in the results shown in Fig. 19. In an extension of the work of Kelly [50], we have developed a smooth interpolation of the EEI parameters that yields reasonable values for the total cross sections throughout the energy region 135–650 MeV spanned by the original six energies. This was accomplished by fitting each of the four strength parameters by a parabolic function. The adjustments were made ''by eye'' so as to achieve a satisfactory repro-duction of the total cross sections while minimizing deviations of the fitted functions from the original parameter sets. The result of this fitting procedure, shown in Table V and in Fig. 20, provides a smooth prescription for EEI calculations in the 135–650 MeV range when combined with the linearly interpolated Franey-Love t matrix. Attempts to extrapolate the interaction below 135 MeV were not successful. In particular, we were unable to find a set of parameters that fit the total cross sections down to 100 MeV, was independent of mass number, and smoothly joined on to the parametrization in the 135–650 MeV region. As a check on the validity of the smoothing procedure, calculations were made of several elastic-scattering angular distributions using both the original EEI parameters and those resulting from the smoothed parameters; agreement was satisfactory. It should be noted that we have not carried out a detailed test of the interpolated interaction against the full set of elastic, inelastic, and analyzing-power data that were used in the development of the original EEI. Such a test would be a useful subject for future work.

Comparison of the neutron total cross sections calculated using the interpolated EEI with results for 18 samples measured in the 1990 and 1996–1997 LANSCE/WNR measurements is shown in Fig. 21. In most cases the calculations lie within a few percent of the experimental data.

The smoothed EEI developed for the neutron total cross sections also yields excellent agreement with proton reaction cross section data without further adjustments. This is shown
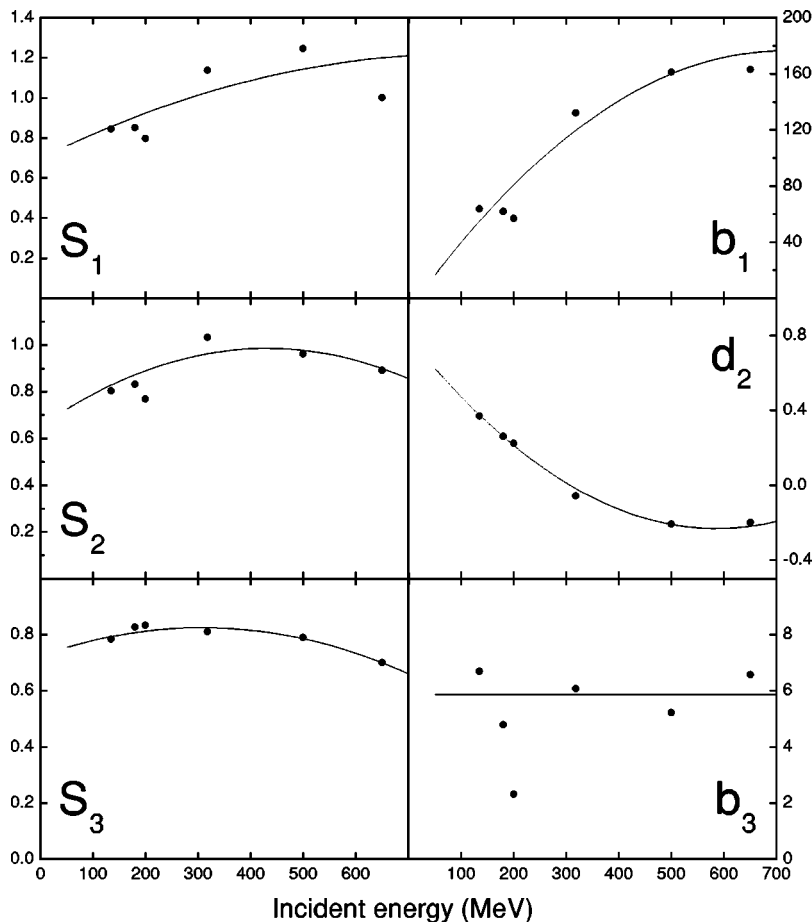

FIG. 20. Comparison of the smoothed EEI parametrization as shown in Table V with the original parameters determined at six energies [29].
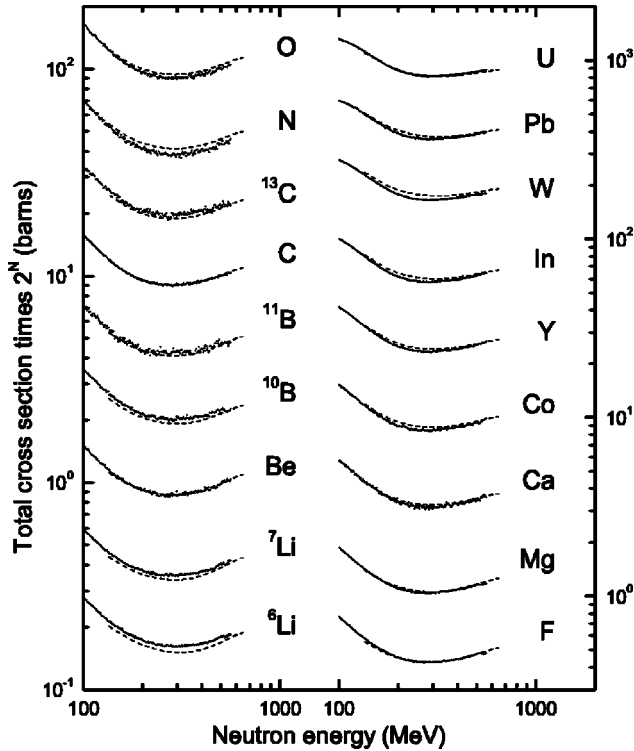
FIG. 21. The dashed lines show neutron total cross sections calculated using the smoothed EEI indicated in Table V. Experimental data are from the 1996–1997 LANSCE/WNR measurements [7], except for Be, N, O from the 1990 measurements [1]. For natural samples the calculations were made using the isotopes indicated in Table IV. The scaling exponent N (see ordinate label) is 0 for the lowest nucleus on each half of the figure (^{6}Li and F) and increases by 1 for each higher nucleus.

in Fig. 22, in which the calculations are compared with the measurements of Renberg *et al.* [30].

D. Conclusions

The extensive body of data from the 1990 and 1996–1997 neutron total cross section measurements has enabled the refinement of an empirical effective interaction based on the work of Kelly and Wallace [29] that varies smoothly with energy over the range 135–650 MeV and appears to be highly useful as a predictive tool. Although developed from proton angular distributions on $T=0$ light nuclei, the interaction provides very good reproduction of both neutron total and proton reaction cross section data over the whole periodic table without adjustments other than the smoothing procedure described above.

At lower energies, the JLM optical potential provides a useful prescription for calculating total cross sections, typically within a few percent in the range 5–80 MeV; above this energy a significant upward normalization of the imaginary potential is necessary, as indicated in Ref. [36]. The wide mass range covered by the present total cross section data indicates the need for an increase in the parameter describing the range of the effective interaction with increasing
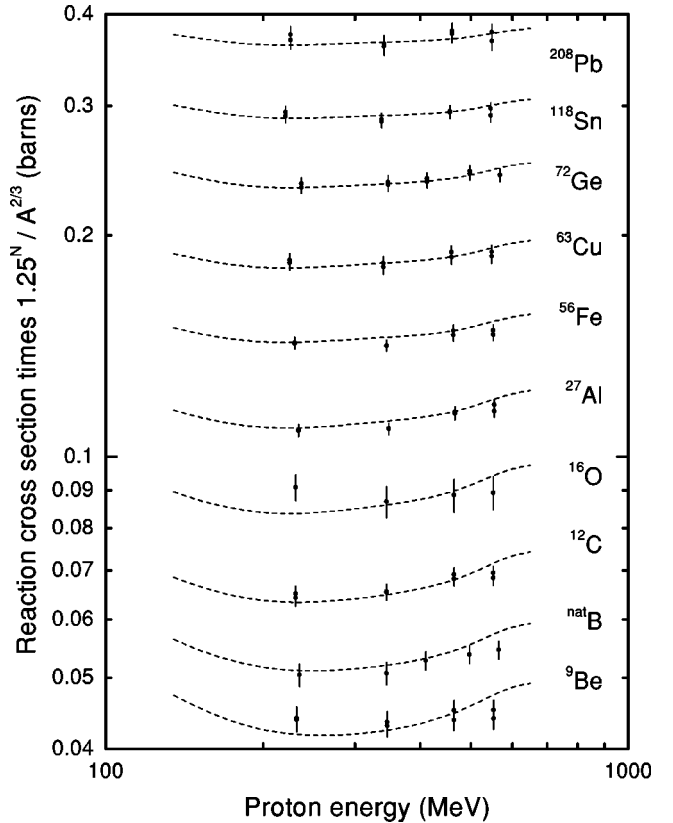

FIG. 22. The dashed lines show proton reaction cross sections calculated using the smoothed EEI indicated in Table V. Experimental data on samples of natural composition are from Renberg *et al.* [30]. The calculations were made for the indicated isotopes, except for ^{nat}B, which was an appropriately weighted combination of ^{10,11}B. The scaling exponent N (see ordinate label) is 0 for Be and increases by 1 for each higher nucleus.

mass and also a slight decrease in the normalizing parameter for the real potential.

The work presented in this paper suggests that the two microscopic folding models employed are sufficiently accurate to provide useful data on total and reaction cross sections for inclusion in codes for spallation-physics applications such as MCNPX in cases where reliable experimental data are lacking. The present implementation of the JLM model can provide data up to about 80 MeV with reasonable accuracy (a few percent). The empirical effective interaction as refined in the present work appears to be very successful in reproducing both total and reaction cross sections well in the range of its validity, 135 to 650 MeV.

[1] R. W. Finlay, W. P. Abfalterer, G. Fink, E. Montei, T. Adami, P. W. Lisowski, G. L. Morgan, and R. C. Haight, Phys. Rev. C **47**, 237 (1993).

[2] S. M. Grimes, J. D. Anderson, R. W. Bauer, and V. A. Madsen, Nucl. Sci. Eng. **130**, 340 (1998).

[3] R. W. Bauer, J. D. Anderson, S. M. Grimes, D. A. Knapp, and V. A. Madsen, Nucl. Sci. Eng. **130**, 348 (1998).

[4] S. M. Grimes, J. D. Anderson, R. W. Bauer, and V. A. Madsen, Nucl. Sci. Eng. **134**, 77 (2000).

[5] W. P. Abfalterer, F. B. Bateman, F. S. Dietrich, Ch. Elster, R. W. Finlay, W. Glöckle, J. Golak, R. C. Haight, D. Hüber, G. L. Morgan, and H. Witała, Phys. Rev. Lett. **81**, 57 (1998).

[6] P. W. Lisowski, C. D. Bowman, G. J. Russell, and S. A. Wender, Nucl. Sci. Eng. **106**, 208 (1990).

[7] W. P. Abfalterer, F. S. Dietrich, R. C. Haight, G. L. Morgan, F. B. Bateman, and R. W. Finlay, ''Measurement of Neutron Total Cross Sections up to 600 MeV in Support of the APT Program,'' Los Alamos Report No. LA-UR-99-666, 1999.

[8] M. S. Moore, Nucl. Instrum. Methods **169**, 245 (1980).

[9] C. Y. Fu and F. G. Perey, Report No. ORNL, 1973.

[10] F. G. Perey, T. A. Love, and W. E. Kinney, Report No. ORNL-4823, 1972.

[11] P. W. Lisowski (private communication).

[12] D. G. Foster, Jr. and D. W. Glasgow, Phys. Rev. C **3**, 576 (1971).

[13] J. D. Kellie, G. P. Lamaze, and R. B. Schwartz, in *Proceedings of the International Conference on Nuclear Cross Sections for Technology*, edited by J. L. Fowler, C. H. Johnson, and C. D. Bowman, NBS Spec. Publ. No. 594, 1980 (U.S. Department of Commerce, Washington, D.C., 1980), p. 48.

[14] J. A. Harvey and N. W. Hill, Report No. ORNL-4937, 187, 1974.

[15] J. A. Harvey, N. W. Hill, and K. Rush, Report No. DOE-NDC-12, 229, 1978.

[16] D. B. Fossan, R. L. Walter, W. E. Wilson, and H. H. Barschall, Phys. Rev. **123**, 209 (1961).

[17] P. W. Lisowski, M. S. Moore, G. L. Morgan, and R. E. Shamu, in *Proceedings of the International Conference on Nuclear Cross Sections for Technology*, [13], p. 524.

[18] J. Franz, H. P. Grotz, L. Lehmann, E. Rössle, H. Schmitt, and L. Schmitt, Nucl. Phys. **A490**, 667 (1988).

[19] N. Nereson and S. Darden, Phys. Rev. **94**, 1678 (1954).

[20] R. B. Schwartz, R. A. Schrack, and H. T. Heaton II, Report No. NBS-MONO-138, 1974.

[21] W. Schimmerling, T. J. Devlin, W. W. Johnson, K. G. Vos-burgh, and R. E. Mischke, Phys. Rev. C **7**, 248 (1973).

[22] D. C. Larson, J. A. Harvey, and N. W. Hill, Report No. ORNL-5787, 174, 1981.

[23] P. W. Lisowski (private communication).

[24] D. Madland and A. Sierk (private communication).

[25] R. W. Finlay and A. E. Feldman, *Proceedings of a Specialists' Meeting on the Nucleon Nucleus Optical Model up to 200 MeV*, Bruyères-le-Châtel, France, 1996, Organization for Economic Cooperation and Development Nuclear Energy Agency (OECD, Paris, France, 1997), No. NEA 0528.

[26] J.-P. Jeukenne, A. Lejeune, and C. Mahaux, Phys. Rev. C **10**, 1391 (1974).

[27] J.-P. Jeukenne, A. Lejeune, and C. Mahaux, Phys. Rev. C **15**, 10 (1977).

[28] J.-P. Jeukenne, A. Lejeune, and C. Mahaux, Phys. Rev. C **16**, 80 (1977).

[29] J. J. Kelly and S. J. Wallace, Phys. Rev. C **49**, 1315 (1994).

[30] P. U. Renberg *et al.*, Nucl. Phys. **A183**, 81 (1972).

[31] H. de Vries, C. W. de Jager, and C. de Vries, At. Data Nucl. Data Tables **36**, 495 (1987).

[32] *Nuclear Sizes and Structure*, edited by R. C. Barrett and D. F. Jackson (Clarendon, Oxford, 1977).

[33] B. Frois *et al.*, Phys. Rev. Lett. **38**, 152 (1977).

[34] G. W. Hoffmann *et al.*, Phys. Rev. C **21**, 1488 (1980).

[35] F. S. Dietrich *et al.*, Phys. Rev. Lett. **51**, 1629 (1983).

[36] E. Bauge, J.-P. Delaroche, and M. Girod, Phys. Rev. C **58**, 1118 (1998).

[37] B. B. P. Sinha *et al.*, Phys. Rev. C **7**, 1930 (1973).

[38] I. Sick, Nucl. Phys. **A218**, 509 (1974).

[39] S. Mellema, R. W. Finlay, F. S. Dietrich, and F. Petrovich, Phys. Rev. C **28**, 2267 (1983).

[40] J. S. Petler, M. S. Islam, R. W. Finlay, and F. S. Dietrich, Phys. Rev. C **32**, 673 (1985).

[41] J. R. M. Annand, R. W. Finlay, and F. S. Dietrich, Nucl. Phys. **A443**, 249 (1985).

[42] L. F. Hansen *et al.*, Phys. Rev. C **31**, 111 (1985).

[43] N. Olsson *et al.*, Nucl. Phys. **A472**, 237 (1987).

[44] A. Lejeune, Phys. Rev. C **21**, 1107 (1980).

[45] R. R. Scheerbaum, Nucl. Phys. **A257**, 77 (1976).

[46] M. A. Franey and W. G. Love, Phys. Rev. C **31**, 488 (1985).

[47] J. A. Carr, J. J. Kelly, and F. Petrovich, computer code ALLWRLD (unpublished).

[48] F. Petrovich, J. A. Carr, and H. McManus, Annu. Rev. Nucl. Part. Sci. **36**, 29 (1986).

[49] F. S. Dietrich, optical-model computer code FOP (unpublished).

[50] J. J. Kelly, Phys. Rev. C **54**, 2547 (1996).